Journal of Solid State Chemistry 184 (2011) 937–944

Contents lists available at ScienceDirect

Journal of Solid State Chemistry

journal homepage: www.elsevier.com/locate/jssc

Structural study and physical properties of a new phosphate $KCuFe(PO_4)_2$

Abdessalem Badri [a], Mourad Hidouri [a,*], María Luisa López [b], Carlos Pico [b], Alain Wattiaux [c], Mongi Ben Amara [a]

[a] UR Matériaux Inorganiques, Faculté des Sciences, 5019 Monastir, Tunisie
[b] Departamento de Química Inorgánica I, Facultad de Ciencias Químicas, Universidad Complutense, 28040 Madrid, Spain
[c] Institut de Chimie de la Matière Condensée de Bordeaux, CNRS,Université de Bordeaux I, 87 Avenue du Dr. A. Schweitzer, 33608 Pessac-Cedex, France

ARTICLE INFO

Article history:
Received 11 January 2011
Received in revised form
16 February 2011
Accepted 16 February 2011
Available online 4 March 2011

Keywords:
Phosphate
X-ray diffraction
Mössbauer spectroscopy
Magnetic susceptibility
Electrical measurements

ABSTRACT

Single crystals of a new phosphate $KCuFe(PO_4)_2$ have been prepared by the flux method and its structural and physical properties have been investigated. This compound crystallizes in the monoclinic system with the space group $P2_1/n$ and its parameters are: $a=7.958(3)$ Å, $b=9.931(2)$ Å, $c=9.039(2)$ Å, $\beta=115.59(3)^\circ$ and $Z=4$. Its structure consists of FeO_6 octahedra sharing corners with Cu_2O_8 units of edge-sharing CuO_5 polyhedra to form undulating chains extending infinitely along the *b*-axis. These chains are connected by the phosphate tetrahedra giving rise to a 3D framework with six-sided tunnels parallel to the [101] direction, where the K^+ ions are located. The Mössbauer spectroscopy results confirm the exclusive presence of octahedral Fe^{3+} ions. The magnetic measurements show the compound to be antiferromagnetic with $C_m=5.71$ emu K/mol and $\theta=-156.5$ K. The derived experimental effective moment $\mu_{ex}=6.76\mu_B$ is somewhat higher than the theoretical one of $\mu_{th}=6.16\mu_B$, calculated taking only into account the spin contribution for Fe^{3+} and Cu^{2+} cations. Electrical measurements allow us to obtain the activation energy (1.22 eV) and the conductivity measurements suggest that the charge carriers through the structure are the potassium cations.

1. Introduction

In the last two decades, an extensive search has been carried out for new ferroelectric, piezoelectric, laser luminescent and other materials, which can be applied in quantum electronics and fiber optics and used as sorbents and catalysts. In this context, complex phosphates containing mono- and trivalent cations are of particular interest [1–3]. The structural properties of these compounds were discussed in detail and it was revealed that the sizes of the M^I and M^{III} cations and their ratio have a dominant role in their structure formation [4].

The targeted synthesis of new phosphates containing variable combinations of cations and predictions of their physico-chemical characteristics require revealing the composition–structure–property relations for different types of compounds. In this sense, the aim of this work is to study the relations between structure and properties of two phosphates, $KMgFe(PO_4)_2$ [5] and $KCuFe(PO_4)_2$. The stoichiometry of these compounds could be related with the $Ca_3(PO_4)_2$ one, where the Ca^{2+} can be substituted by various cations [6] and with the $Ca_3(VO_4)_2$ one which is a high temperature ferroelectric (FE) with a phase transition temperature of $T_c=1383$ K [7]. Other compounds of this type, e.g. $Ca_9R(PO_4)_7$ also possess ferroelectric (FE) phase transitions [8]. Sr-analogs of such phosphates, $Sr_9R(PO_4)_7$ have been shown to have a centrosymmetric monoclinically distorted β-$Ca_3(PO_4)_2$-type structure [9]. This compound exhibits an antiferroelectric (AFE) phase transition at 773 K [10].

In this paper, we report the synthesis, structural characterization and physical properties of a new phosphate $KCuFe(PO_4)_2$, and the electrical behavior is compared with $KMgFe(PO_4)_2$ which shows a bi-dimensional structure as we have recently reported [5].

2. Experimental section

2.1. Synthesis

Single crystals of $KCuFe(PO_4)_2$ were prepared by crystallization in a flux of potassium dimolybdate $K_2Mo_2O_7$, in an atomic ratio P:Mo=4:1. Appropriate amounts of KNO_3 (Fluka, 99%), $Cu(NO_3)_2\cdot 6H_2O$ (Acros, 99%), $Fe(NO_3)_3\cdot 9H_2O$ (Fisher, 98.6%), $(NH_4)_2HPO_4$ (Merck, 99%) and MoO_3 (Acros, 99%) were mixed by dissolving in aqueous nitric acid and the obtained solution was dried at 353 K. The resulting dry residue was ground in an agate mortar to ensure its best homogeneity, and then gradually heated

* Corresponding author.
E-mail address: mourad_hidouri@yahoo.fr (M. Hidouri).

0022-4596/$ - see front matter © 2011 Elsevier Inc. All rights reserved.
doi:10.1016/j.jssc.2011.02.021

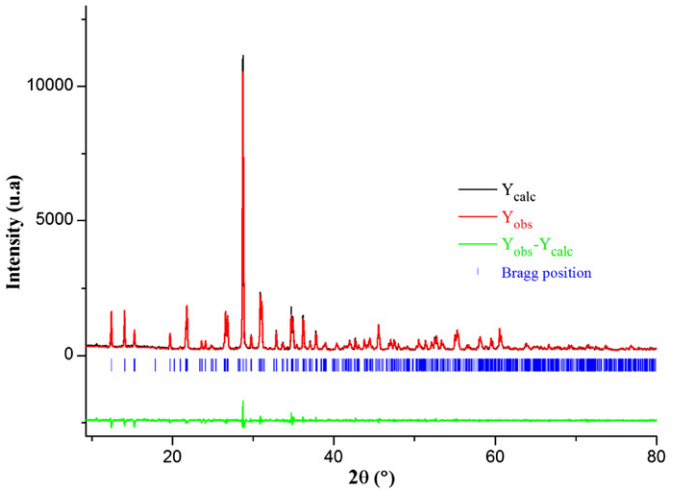

Fig. 1. The powder X-ray diagram of $KCuFe(PO_4)_2$.

Table 1
Details of the data collection and structural refinement for $KCuFe(PO_4)_2$.

Crystal data	
Chemical formula	$KCuFe(PO_4)_2$
Crystal system	Monoclinic
Space group	$P2_1/n$
a (Å)	7.958(3)
b (Å)	9.931(2)
c (Å)	9.039(2)
β (deg.)	115.59(3)
Z	4
ρ_{cal} (g cm^{-3})	3.59
Data collection	
Crystal dimensions	$0.4 \times 0.1 \times 0.1$ mm
Diffractometer	CAD4 (Enraf-Nonius)
Radiation	λ (Mo $K\alpha$)=0.7107 Å
Monochromator	Graphite
μ (mm^{-1})	6.7
Scan type	$\omega/2\theta$
Scan speed	Variable
$2\theta_{max}$ (deg.)	59.9
Number of unique reflections; R_{int}	1872; R_{int}=0.031
Number of observed reflections [$I > 2\sigma(I)$]	1771
F (000)	672
Structural refinement	
Intensity corrections	Lorentz–polarization
Absorption correction ($T_{min,\ max}$)	Analytical (0.20, 0.49)
Structure solution	Direct methods
Reliability factors	R_1=0.028; wR_2=0.089; S=0.98
Number of parameters	119
$(\Delta\rho)_{max,\ min}$ (e Å^{-3})	0.97; −0.84

up to 873 K in a platinum crucible. After being reground, the mixture was melted for 1 h at 1173 K and subsequently cooled at a rate of 10 K h^{-1} down to 673 K, after which the furnace was turned off. The crystals obtained by washing the final product with warm water, in order to dissolve the flux, are essentially composed by dark green and hexagonally shaped rod crystals of $KCuFe(PO_4)_2$.

After the structure determination, a polycrystalline sample was synthesized by a conventional solid state reaction starting from a stoichiometric mixture of KNO_3, $Cu(NO_3)_2 \cdot 6H_2O$, $Fe(NO_3)_3 \cdot 9H_2O$ and $(NH_4)_2HPO_4$. After an initial treatment, similar to that undertaken for the synthesis of the single crystals until 873 K, the sample was subjected to final calcinations at 1113 K for

Table 2
Atomic coordinates and displacement parameters U_{eq} (Å^2) for $KCuFe(PO_4)_2$.

Atom	*Wyckoff*	*x*(σ)	*y*(σ)	*z*(σ)	U_{eq} (σ)
K	8*d*	0.4179(2)	−0.1333(1)	0.0748(1)	0.0239(2)
Cu	8*d*	0.3695(1)	0.1201(2)	−0.5532(1)	0.0077(2)
Fe	8*d*	0.0143(1)	0.1253(1)	−0.2573(1)	0.0051(2)
P1	8*d*	0.1281(1)	0.1594(1)	−0.8587(1)	0.0050(2)
O11	8*d*	0.4496(2)	0.2635(2)	−0.3942(2)	0.0097(3)
O12	8*d*	0.3000(2)	0.2464(2)	−0.7429(2)	0.0075(3)
O13	8*d*	0.1483(2)	0.0375(2)	−0.7424(2)	0.0083(3)
O14	8*d*	0.1426(3)	0.1141(2)	−0.0127(2)	0.0096(3)
P2	8*d*	0.2677(2)	−0.0886(1)	−0.3511(1)	0.0047(2)
O21	8*d*	0.0970(3)	−0.1312(2)	−0.5042(2)	0.0100(3)
O22	8*d*	0.3580(3)	−0.2084(2)	−0.2403(2)	0.0090(3)
O23	8*d*	0.2221(2)	0.0137(2)	−0.2469(2)	0.0092(3)
O24	8*d*	0.4148(3)	−0.0236(2)	−0.3993(2)	0.0090(3)

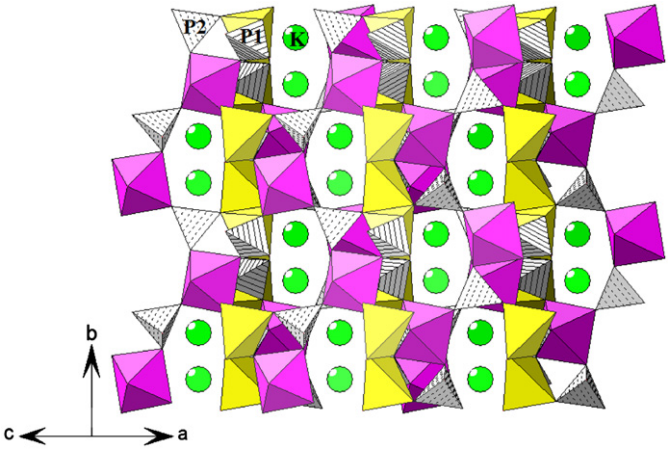

Fig. 2. A projection along the [101] direction of the structure showing the six-edged tunnels, occupied by the K^+ ions. *Legend*: CuO_5 polyhedra=yellow; PO_4 tetrahedra=hatched; FeO_6 polyhedra=purple; and K^+ cations=green circles. (For interpretation of the references to color in this figure legend, the reader is referred to the web version of this article.)

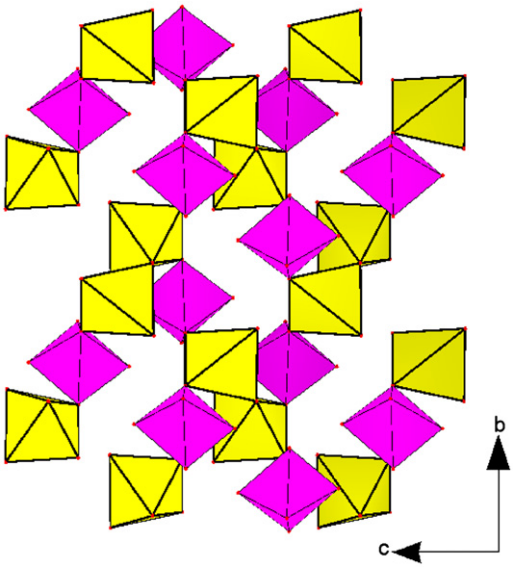

Fig. 3. The Cu/Fe/O sub-network forming sheet parallel to the *bc* plane. *Legend*: CuO_5 polyhedra=yellow and FeO_6 polyhedra=purple. (For interpretation of the references to color in this figure legend, the reader is referred to the web version of this article.)

48 h with intervening grinding. A light green powder was obtained by quenching in air. Its purity was checked from the examination of its X-ray powder diagram (Fig. 1) collected in the range $5^\circ \leq 2\theta \leq 80^\circ$ on a PANalytical diffractometer using Cu$K\alpha$ radiation ($\lambda = 1.5406$ Å).

2.2. Structure determination

The structure was determined from single CRYSTAL X-ray DIFFRACTION data, collected at room temperature by an Enraf-Nonius CAD4 diffractometer using monochromated Mo-$K\alpha$ radiation ($\lambda = 0.7107$ Å) and $\omega/2\theta$ scans. The unit cell parameters and the orientation matrix were determined from a least-squares fit of 25 reflections in the range $9.08^\circ \leq \theta \leq 12.69^\circ$. A total of 1872 unique reflections measured with a maximum 2θ of 60° for the $(-h,-k,\pm l)$ hemisphere ($R_{in}=0.031$) but only 1771 were considered as observed according to the statistic criterion [$I > 2\sigma(I)$]. The systematic absences $k=2n+1$ for 0 k 0 and $h+l=2n+1$ for h 0 l indicated the monoclinic space group $P2_1/n$. The intensity data were corrected for Lorentz and polarization effects. Absorption corrections were done analytically taking into account the size and shape of the crystal ($T_{min}=0.20$; $T_{max}=0.49$). The structure was solved by direct methods [11], which allowed the positions of the Cu, Fe and K atoms to be determined. The P and O atoms were subsequently localized by inspection of the difference electron density maps [12]. A final refinement cycle using all atomic position and including anisotropic displacement parameters led to the reliability factors $R_1=0.028$ and $wR_2=0.087$. The cationic distribution was confirmed by a Bond Valence Sums (B. V. S.) calculation using the Brown and Altermatt method [13]. Experimental conditions for intensity measurements, structure solution and refinement are reported in Table 1. Final atomic coordinates and equivalent isotropic displacement parameters are listed in Table 2.

2.3. Characterization

A Mössbauer spectrum was recorded at room temperature on a constant acceleration HALDER-type spectrometer using a room temperature ^{57}Co source [Rh matrix] in transmission geometry. Samples were prepared with a thickness of about 10 mg cm^{-2} of iron to avoid the experimental widening of the peaks. The velocity was calibrated using pure iron metal as a standard material. The isomer shift is given with respect to α-Fe.

The magnetic susceptibility measurements were carried out in the 2–300 K temperature range under a constant applied field of 500 Oe by a Quantum Design SQUID magnetometer. The independence of the susceptibility value with regard to the applied field up to 50 kOe was checked at 2 K.

Electrical properties have been performed from the analysis of ac complex impedance spectroscopy. A Solartron SI 1260 impedance/gain-phase Analyzer was used with frequencies ranging from 1 Hz to 10 MHz in the temperature regions 300–673 K. Cylindrical pellets were prepared by compressing the powder (5 ton) to 1.32 mm in height and 13 mm in diameter. The pellet was sintered at 973 K during 48 h and coated with platinum paint on both sides.

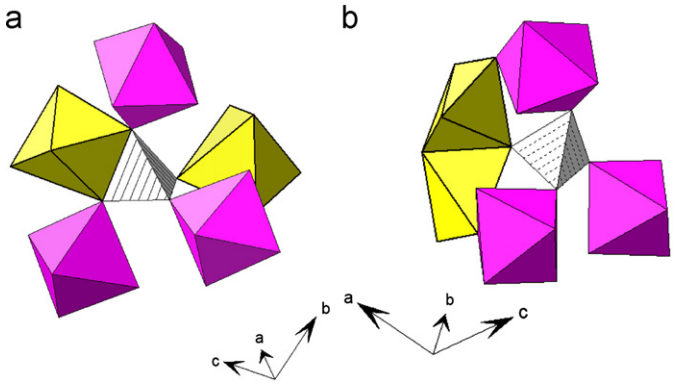

Fig. 4. The polyhedral environments of the P(1)O_4 (a) and P(2)O_4 tetrahedra (b). *Legend*: CuO_5 polyhedra=yellow; PO_4 tetrahedra=hatched; and FeO_6 polyhedra=purple. (For interpretation of the references to color in this figure legend, the reader is referred to the web version of this article.)

Table 3
Main interatomic distances (Å) at angles (deg.) for $KCuFe(PO_4)_2$.

CuO_5			
Cu–O(24)	1.916(1)	O(24)–Cu–O(11)	96.4(1)
Cu–O(11)	1.922(2)	O(24)–Cu–O(12)	170.2(1)
Cu–O(12)	2.000(2)	O(11)–Cu–O(12)	93.2(1)
Cu–O(13)	2.024(2)	O(24)–Cu–O(13)	97.7(1)
Cu–O(24)	2.165(2)	O(11)–Cu–O(13)	144.8(1)
〈Cu–O〉	2.005(2)	O(12)–Cu–O(13)	73.3(1)
		O(24)–Cu–O(24)	84.1(1)
		O(11)–Cu–O(24)	116.1(1)
		O(12)–Cu–O(24)	93.3(1)
		O(13)–Cu–O(24)	97.3(1)
FeO_6			
Fe–O(22)	1.943(2)	O(22)–Fe–O(21)	82.3(1)
Fe–O(21)	1.946(2)	O(22)–Fe–O(23)	92.6(1)
Fe–O(23)	1.959(2)	O(21)–Fe–O(23)	92.3(1)
Fe–O(14)	1.999(2)	O(22)–Fe–O(14)	92.3(1)
Fe–O(13)	2.070(2)	O(21)–Fe–O(14)	176.5(1)
Fe–O(16)	2.177(2)	O(23)–Fe–O(14)	84.2(1)
〈Fe–O〉	2.015(2)	O(22)–Fe–O(13)	173.2(1)
		O(21)–Fe–O(13)	92.1(1)
		O(23)–Fe–O(13)	94.1(1)
		O(14)–Fe–O(13)	88.7(1)
		O(22)–Fe–O(12)	86.0(1)
		O(21)–Fe–O(12)	93.2(1)
		O(23)–Fe–O(12)	174.3(1)
		O(14)–Fe–O(12)	90.3(1)
		O(13)–Fe–O(12)	87.2(1)
P(1)O_4			
P(1)–O(14)	1.514(2)	O(14)–P(1)–O(11)	112.9(2)
P(1)–O(11)	1.521(2)	O(14)–P(1)–O(13)	111.2(2)
P(1)–O(13)	1.565(2)	O(11)–P(1)–O13	110.3(2)
P(1)–O(12)	1.574(2)	O(14)–P(1)–O(12)	112.7(2)
〈P(1)–O〉	1.543(2)	O(11)–P(1)–O(12)	109.2(2)
		O(13)–P(1)–O(12)	99.8(1)
P(2)O_4			
P(2)–O(22)	1.521(2)	O(22)–P(2)–O(21)	111.3(2)
P(2)–O(21)	1.522(2)	O(22)–P(2)–O(23)	106.5(2)
P(2)–O(23)	1.531(2)	O(21)–P(2)–O(23)	112.8(2)
P(2)–O(24)	1.554(2)	O(22)–P(2)–O(24)	108.1(2)
〈P(2)–O〉	1.532(2)	O(21)–P(2)–O(24)	110.2(2)
		O(23)–P(2)–O(24)	107.7(2)
KO_9			
K–O(22)	2.779(2)	K–O(12)	3.003(2)
K–O(11)	2.854(2)	K–O(23)	3.017(2)
K–O(23)	2.861(2)	K–O(24)	3.017(2)
K–O(11)	2.914(2)	K–O(14)	3.158(2)
K–O(21)	2.981(2)	〈K–O〉	2.953(2)

3. Results

3.1. Description of the structure

$KCuFe(PO_4)_2$ displays a new type of structure. The asymmetric unit contains 13 atomic positions including one for the K atoms, one for the Cu atoms, one for the Fe atoms, two for the P atoms and eight for the O ones. All these positions are occupying general

positions of space group $P2_1/n$. A projection of this structure along the [101] direction shows the 3D character of the $[CuFe(PO_4)_2]_\infty$ framework forming distorted hexagonal tunnels where are located the K^+ ions (Fig. 2). This framework is composed by four crystallographically distinct building blocks: one Cu_2O_8 unit of edge-sharing CuO_5 polyhedra, one FeO_6 octahedron and two PO_4 tetrahedra. The Cu and Fe polyhedra form rigid sheets laying parallel to the *bc* plane (Fig. 3). In such sheets, one can formally isolate undulating chains of alternating Cu_2O_8 units and FeO_6 octahedra that run parallel to the *b* direction. Successive chains are connected through common corners of their polyhedra. The inter-sheets space is filled by the $P(1)O_4$ and $P(2)O_4$ tetrahedra, which display different connectivity fashions to the Cu and Fe polyhedra (Fig. 4). Each $P(1)O_4$ tetrahedron shares one edge with one CuO_5 polyhedron and four corners, one with a CuO_5 unit and three with three FeO_6 octahedra. Each $P(2)O_4$ tetrahdron shares three corners with three FeO_6 octahedra while the remaining corner is doubly shared with two CuO_5 polyhedra forming a Cu_2O_8 unit.

Main interatomic distances and angles are listed in Table 3. The FeO_6 octahedron is highly distorted in view of the great discrepancy of Fe–O distances varying between 1.943(2) and 2.177(2) Å. The mean ⟨Fe–O⟩ distance of 2.015 Å is, however, consistent with those of 2.017 and 2.025 Å observed for octahedral Fe^{3+} ions in $K_3Fe(PO_4)_2$ [14].

The CuO_5 polyhedron is also highly deformed with one longer Cu–O distance of 2.164(2) Å compared to the four others (from 1.915(2) to 2.023(2) Å). Such a distortion can be attributed to the Jahn Teller effect often observed for Cu^{2+} ions with d^9 configuration. The mean ⟨Cu–O⟩ distance of 2.005(2) Å is consistent with that observed for five coordinated Cu^{2+} ions in $Na_{1/2}Cu_{4/3}Fe_2(PO_4)_3$ [15].

The P–O distances have mean values of 1.534(2) Å for P(1) and 1.532(2) Å for P(2), close to those of monophosphate groups [16].

The K^+ ions occupy a single distinct site within the tunnels. As often observed for alkali ions, its oxygen environment displays a wide range of cation–oxygen distances, thus it is very difficult to distinguish between bonding and non-bonding contacts. A simple criterion is to consider all distances shorter than the shortest K^+ cation distance. Assuming this criterion, this environment consists of nine O atoms with K–O distances ranging from 2.778(2) to 3.159(2) Å.

3.2. Mössbauer spectroscopy

The room temperature Mössbauer spectrum shown in Fig. 5 consists of a single quadrupolar doublet, assigned to a single

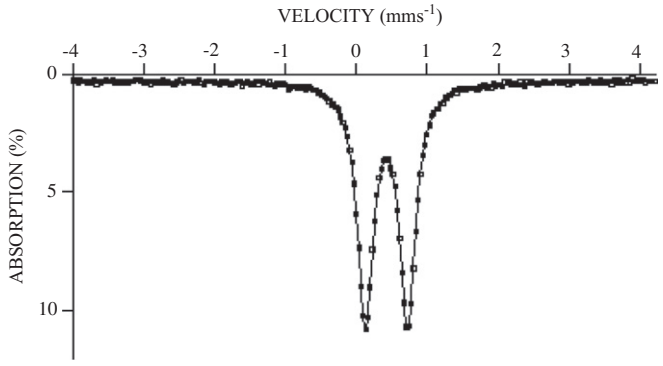

Fig. 5. The room temperature ^{57}Fe Mössbauer spectrum for $KCuFe(PO_4)_2$.

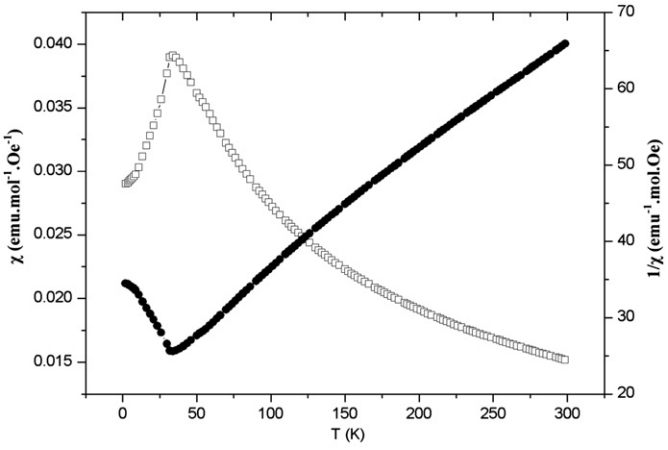

Fig. 6. Magnetic and the reciprocal susceptibilities versus temperature for $KCuFe(PO_4)_2$.

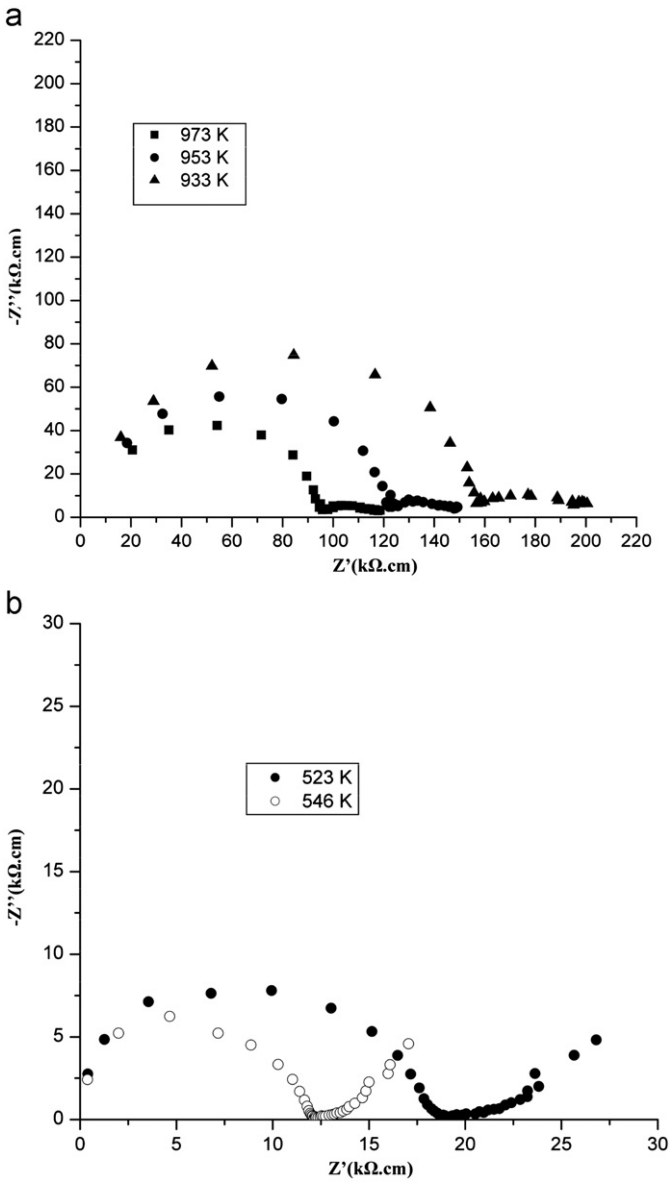

Fig. 7. Nyquist plots at different temperatures for $KCuFe(PO_4)_2$(a) and $KMgFe(PO_4)_2$ (b).

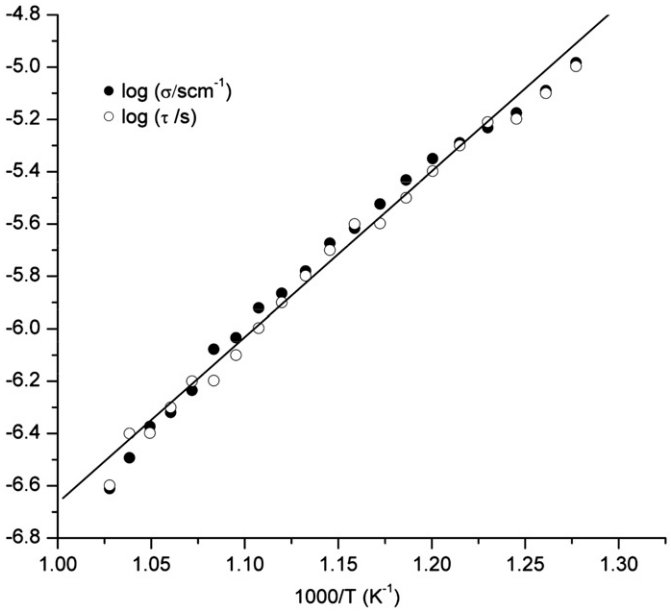

Fig. 8. Conductivity and relaxation time variation vs 1000/T for $KCuFe(PO_4)_2$.

crystallographic site in the structure. This result indicates that there is no supercell, as revealed by the X-ray study.

The obtained isomer shift $\delta=0.442(2)$ mm s^{-1} is in the range 0.40–0.5 mm s^{-1} expected for high spin Fe^{3+} ions in an octahedral site [17]. The high value of the quadrupolar splitting ($\Delta=0.601(2)$ mm s^{-1}) confirms the strong deformation of the FeO_6 octahedron as evident from the structure refinement.

3.3. Magnetic susceptibility

Variable temperature susceptibility measurements for $KCuFe(PO_4)_2$ have been carried out on a powdered sample in the 4.2–300 K temperature range. Fig. 6 shows the temperature dependence of the magnetic and the reciprocal susceptibilities. Above 50 K, the thermal evolution of χ_m follows a Curie–Weiss law, $\chi=C/(T-\theta)$, with $C_m=5.71$ emu K/mol and $\theta=-107.75$ K, calculated in the range 50–150 K. The experimental magnetic moment is 6.76μ_B that is close to the theoretical value of 6.16μ_B, taking only into account the spin contribution for Fe^{3+} and Cu^{2+} cations. These expected values are obtained considering that the paramagnetic regime is simply the superposition of Fe and Cu sub-structures, i.e. the total Curie constant results from the addition of both of Fe and Cu ones. The theoretical magnetic

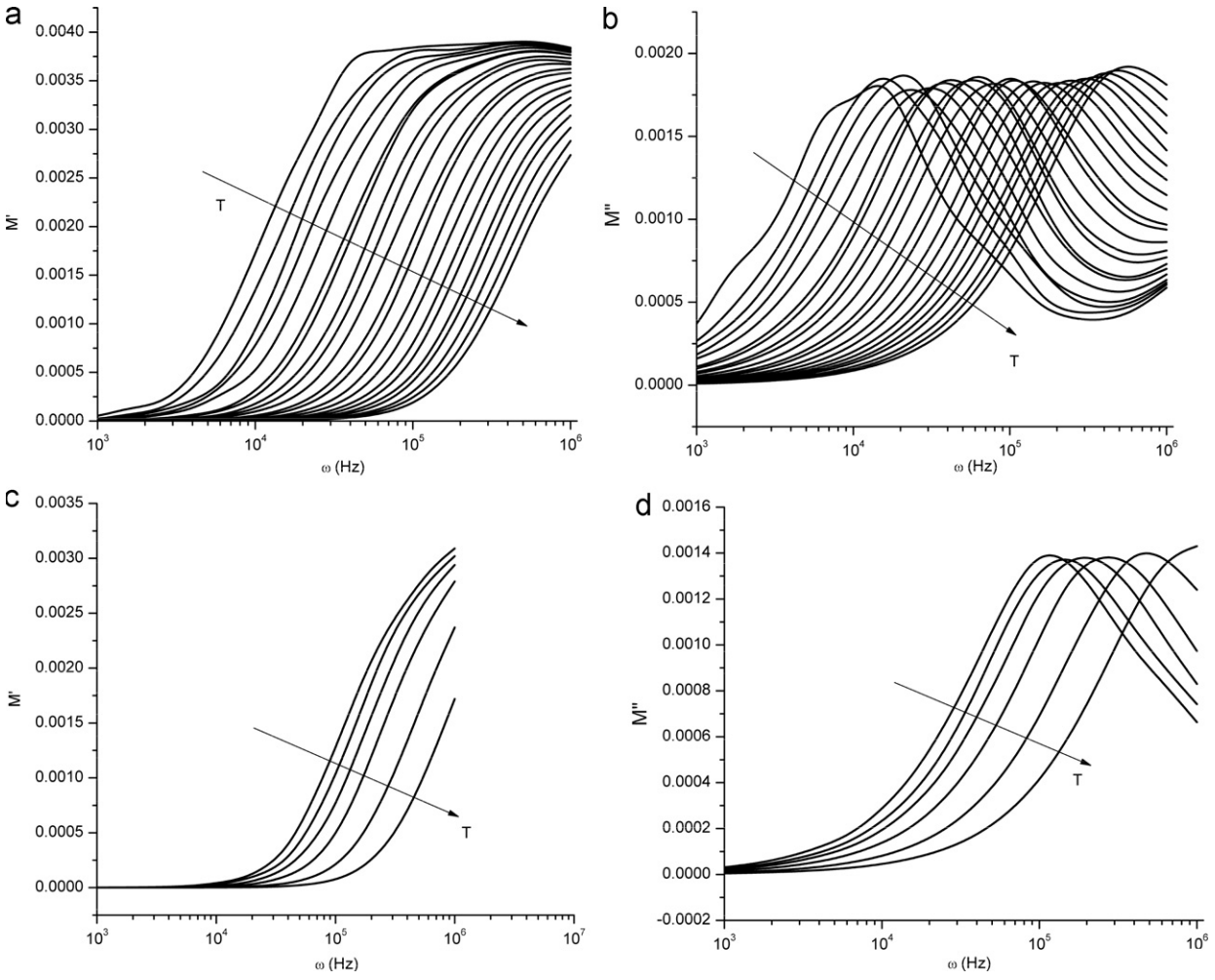

Fig. 9. (a) M' and (b) M'' versus frequencies for $KCuFe(PO_4)_2$ at temperatures between 773 and 973 K; and (c) M' and (d) M'' versus frequencies for $KMgFe(PO_4)_2$ at temperatures between 403 and 523 K. The temperature of each curve increases 10 K following the arrow.

moment can also be calculated following the expressions:

$C_t = C_{Cu}^{2+} + C_{Fe}^{3+}$

$\mu_t = (8C_t)^{1/2}$

It is interesting to note that the sign of the Weiss constant points to AFM interactions at low temperatures, as is also evidenced by the maximum, centered at 36 K that appears in the magnetic susceptibility graph (Fig. 6).

3.4. Electrical behavior

Impedance spectroscopy is widely used to investigate the dielectric and electric properties of ceramics, in our case pellets of the title phosphates, $KMgFe(PO_4)_2$ and $KCuFe(PO_4)_2$ which show very different structural characteristics. From the dielectric response one can obtain, among others, important information on the relaxation processes taking place in the system. The $KMgFe(PO_4)_2$ crystallizes in the *C*2/*c* space group and presents a bi-dimensional structure [5]; the structure of the second one is described above.

Fig. 7 shows impedance plots for both compounds in air using Pt electrodes. Cole–Cole plots of $KMgFe(PO_4)_2$ show a semicircle at high frequencies followed by a spike in the low frequency region. The equivalent circuit used to fit the complex impedance data consists of parallel RC elements with additional constant phase elements (CPE). The obtained capacity value was 6.6×10^{-12} F that is indicative of the bulk response. The low frequency spike can be assigned to space charge polarization or to the Warburg impedance, being characteristic of ionic conductors. In the same figure we can observe the Nyquist plot for $KCuFe(PO_4)_2$, which shows a slightly different shape. In the Z^* plot two resolved semicircle arcs spanning the whole frequency range are obtained. This behavior could be best modeled by invoking an equivalent circuit consisting of a series of two constant phase elements (instead of ideal capacitors) connected in parallel to the resistors. The dispersive frequency dependent capacitance associated with a CPE element is given by $C(\omega)=A(j\omega)^{-\alpha}$, where A is independent of a frequency constant and α is a measure of the distribution of relaxation times [18,19]. According to this relation, $\alpha=0$ represents an ideal capacitor behavior and $\alpha > 0$ values are attributed to the capacitance dispersion owing to the electrical heterogeneity in the sample or to electrode polarization behavior. An impedance analysis software Z-VIEW was used to model the impedance spectra and the capacitances, resistances and exponent values were directly obtained from the fit. Capacitance values of C_1 are between 6.16 and 8.03 pF and these values are nearly constant with the temperature and suggest that the relaxation is due to bulk of the materials. The exponent α_1 for the CPE element, representing the bulk component, takes values of $\sim$0.06 that decrease to 0 with the decrease in temperature indicating a nearly ideal capacitive behavior. On the other hand, at low frequencies, the C_2 values are between 5.02×10^{-7} and 1.87×10^{-6} F with α_2 values that change from 0.52 to 0.76. These values are indicative that the grain boundary component and electrode polarization phenomena overlap.

The conductivity data for $KCuFe(PO_4)_2$ were extracted from the corresponding resistance values obtained from the fit. The variation in bulk conductivity with the temperature (Fig. 8) follows an Arrhenius behavior described as

$\sigma = \sigma_0 \exp(-E_a/kT)$

The activation energy $E_a=1.22$ eV is obtained from the linear fit. In the case of $KMgFe(PO_4)_2$ the corresponding value was noticeably lower, $E_a=0.51$ eV. The difference between both compounds can be related to the structure characteristics in both cases.

The dielectric properties of materials can be expressed in various ways, using different representations. Although these alternative representations are equally valid [20], they may often provide new insight into the dielectric and electrical properties of materials. For example, a comparison of the complex dielectric permittivity, ε^*, and electrical modulus, M^*, representation allows us to distinguish the local dielectric relaxation (e.g., dipole reorientation) from long-range electrical conductivity. Based on values of the activation energies and the characteristic relaxation times, it is possible to ascribe a given process to a specific mechanism. To achieve this purpose, we have applied different representations to analyze the dielectric data in the title compounds whose structures are very different. $KMgFe(PO_4)_2$ phosphate shows a 2D-structure and the mobility of the K^+ cations is more feasible [5] whereas the $KCuFe(PO_4)_2$ compound possesses a 3D structure and therefore the mobility of the K^+ cations is highly difficult.

From the physical point of view, the electrical modulus corresponds to the relaxation of the electrical field in the material

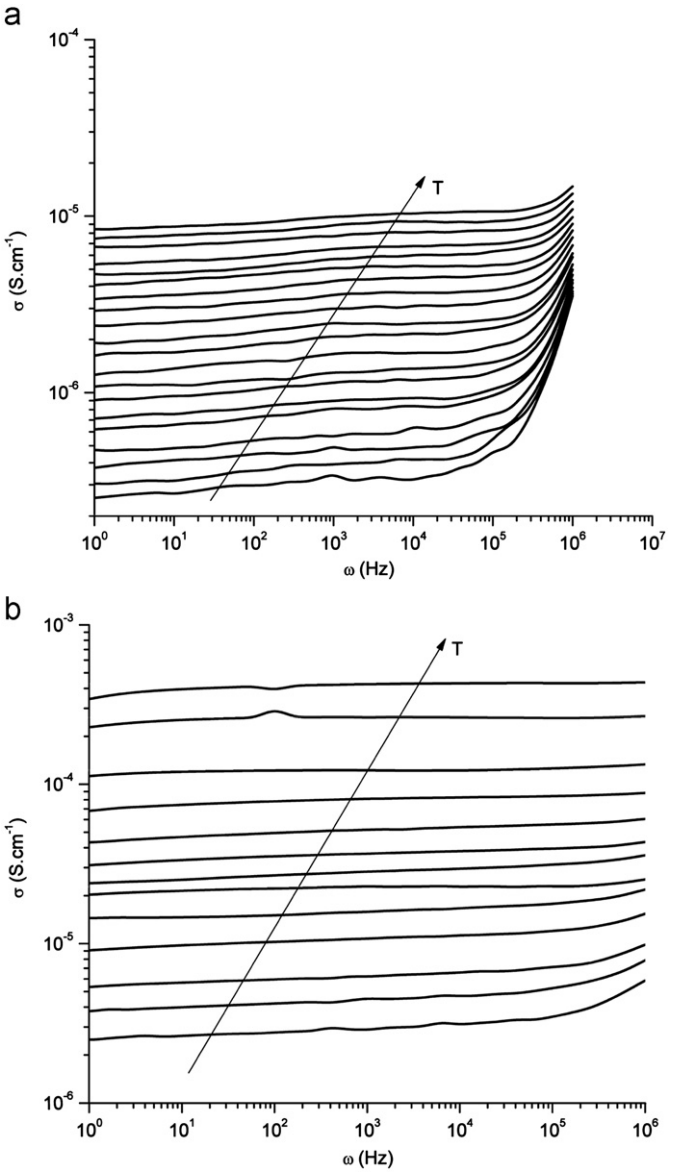

Fig. 10. Ac conductivity versus frequencies for: (a) $KCuFe(PO_4)_2$ at temperatures between 773 and 973 K and (b) $KMgFe(PO_4)_2$ at temperatures between 403 and 523 K. The temperature of each curve increases 10 K following the arrow.

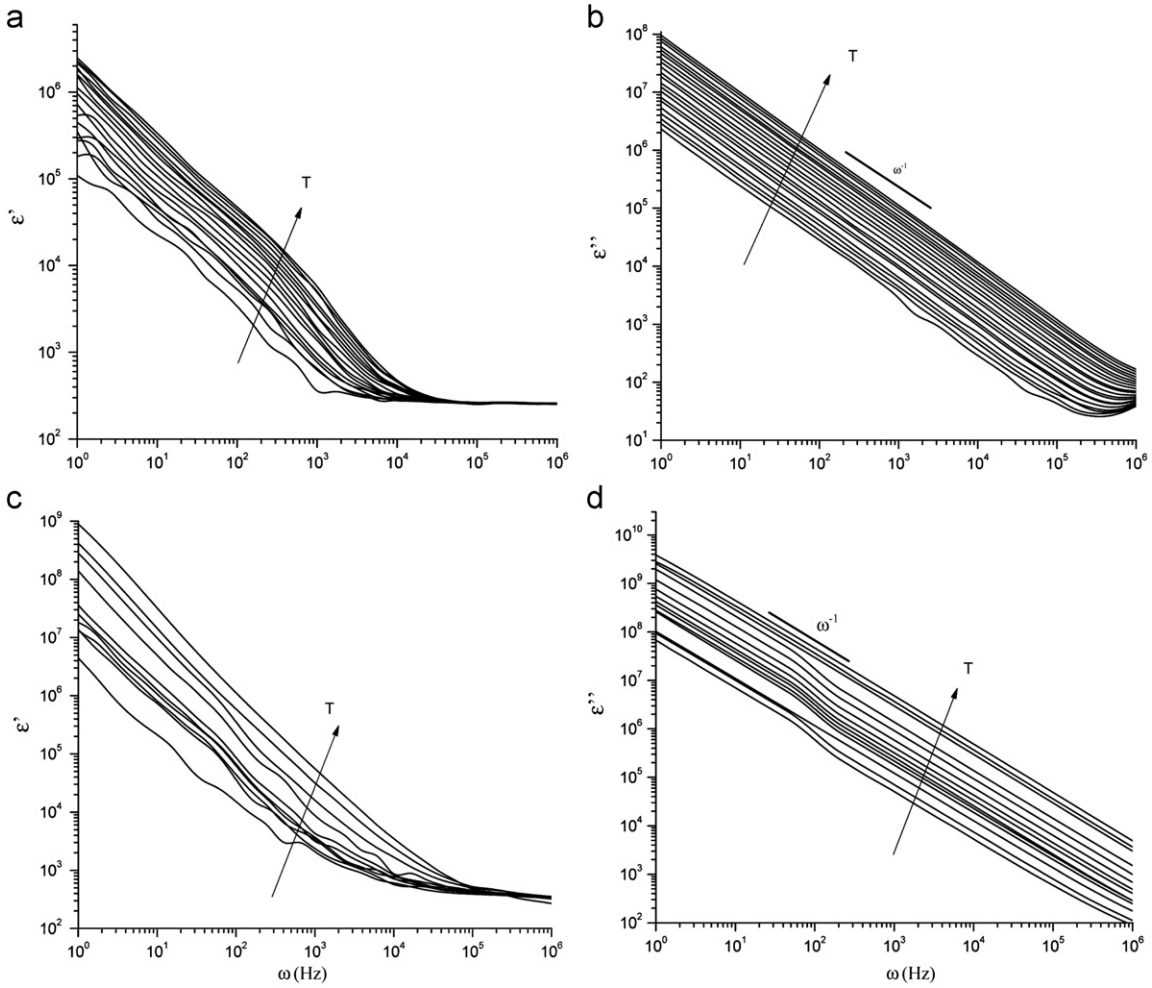

Fig. 11. Variations of: (a) ε' and (b) ε'' versus frequencies for $KCuFe(PO_4)_2$ at temperatures between 773 and 973 K; and (c) ε' and (d) ε'' versus frequencies for $KMgFe(PO_4)_2$ at temperatures between 403 and 523 K. The temperature of each curve increases 10 K following the arrow.

when the electrical displacement remains constant. Therefore, the modulus represents the real dielectric relaxation process [21]. The complex modulus $M^*(\omega)$ was introduced to describe the dielectric response of non-conducting materials. This formalism has been applied also to materials with non-zero conductivity. The usefulness of the modulus representation in the analysis of relaxation properties was demonstrated both for vitreous ionic conductors [22] and polycrystalline ceramics [23].

3.4.1. Modulus spectra

The modulus spectra are depicted in Fig. 9a and b for both compounds. Data presented in this way exhibit a pronounced relaxation peak for $M''(\omega)$ that moves towards lower frequencies during the sample cooling. Consequently, it means that the relaxation rate for this process increases with decreasing temperature. As a convenient measure of the characteristic relaxation time one can choose the inverse of frequency of the maximum peak position, i.e. $\tau=(2\pi f_{max})^{-1}$. Thus, we can determine the temperature dependence of the characteristic relaxation time straightforwardly, as shown in Fig. 8 for both phosphates. These relaxation times satisfy an almost linear dependence in accordance with the Arrhenius law:

$$\tau_M = \tau_{0,M} \exp\left(\frac{E_{A,M}}{kT}\right)$$

From the numerical fitting analysis, we found values of activation energy, $E_{A,M}$=0.47 and 1.20 eV and the conductivity characteristic relaxation times, $\tau_0=2\times10^{-12}$ and 2×10^{-13} for $KMgFe(PO_4)_2$ and $KCuFe(PO_4)_2$, respectively. These τ_0 values may indicate the ionic process and this quantity is higher in the 2D phosphate than in the 3D one as it was expected.

The activation energy calculated from relaxation time, $E_{a,M}$, is attributed to the long-range movement of free charge carriers, K^+, that behave as free ions. On the other hand, the trend in the variation in τ_M with reciprocal temperature is very similar to that of conductivity, suggesting that the dielectric screening arise from the same charge carriers that contribute to the electrical conductivity, in agreement with the behavior observed in Fig. 8.

The frequency dependent conductivity $\sigma(\omega)$ is depicted in Fig. 10 for both compounds. The $\sigma(\omega)$ follows a universal dielectric response behavior governed by

$$\sigma = \sigma_0 + A(T)\omega^n$$

where σ_0 is the bulk dc conductivity and $A(T)$ and n are temperature dependent constants. From the σ_{dc} results together with the σ ones, obtained from the equivalent circuit, we can observe the good match between both sets of values. The high frequency conductivity is entirely due to the hopping of localized carriers.

3.4.2. Dielectric permittivity

In the frequency domain, the dielectric response of the system subjected to an external oscillating electric field is fully characterized by the complex permittivity, $\varepsilon^*=\varepsilon'(\omega)+i\varepsilon''(\omega)$, where the real and imaginary components are the storage and loss, respectively,

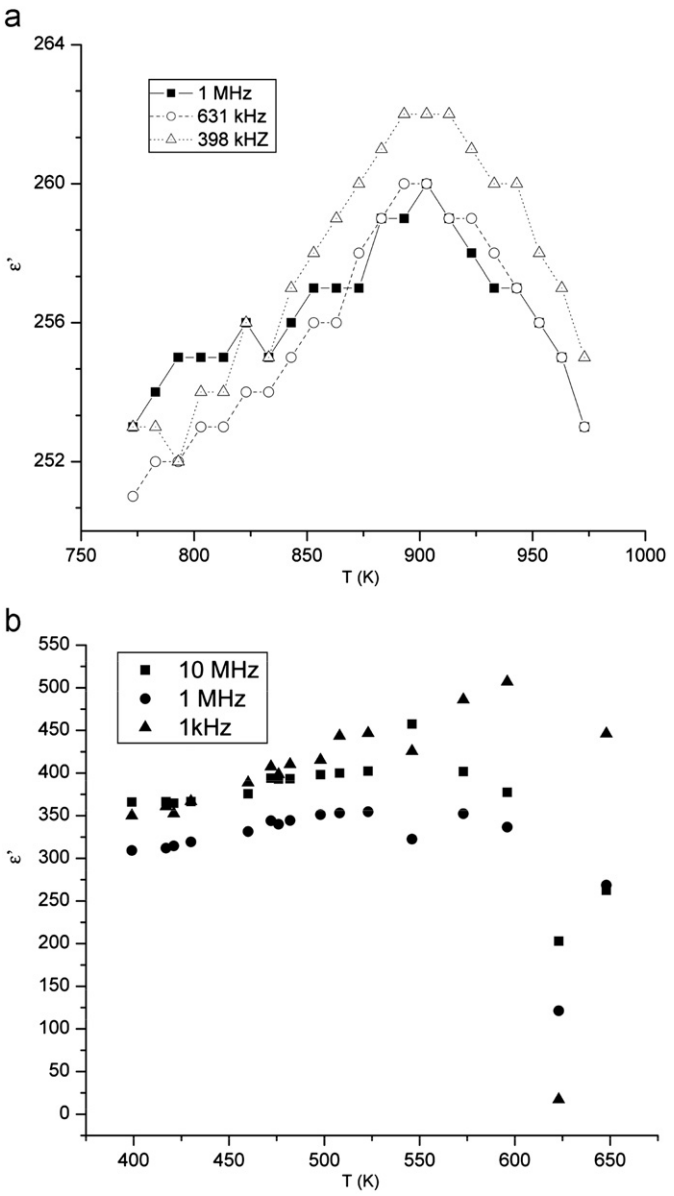

Fig. 12. Real permittivity vs temperature for (a) $KCuFe(PO_4)_2$ and (b) $KMgFe(PO_4)_2$.

of the energy during each cycle of the electric field. Fig. 11 shows the frequency dependence of real and imaginary parts of the complex dielectric permittivity for $KCuFe(PO_4)_2$ and $KMgFe(PO_4)_2$. An upward trend in $\varepsilon''(\omega)$ is attributed entirely to dc-conductivity. This part of dielectric losses follows a ω^{-1} dependence according to the electrodynamics relation $\varepsilon''(\omega)=\sigma_{dc}/\varepsilon_0\omega$. However, this frequency dependence is followed in all frequency range for the phosphate $KMgFe(PO_4)_2$ but a clear dispersion for highest frequencies is observed in $KCuFe(PO_4)_2$. Both samples show a similar response in the real part of permittivity with a plateau at the highest frequencies followed by dispersion at lower frequencies. This response is characteristic of ionic conductivity.

Permittivity data are shown as a function of temperature in Fig. 12 for different frequencies. These results evidence that they are independent of temperature for $KMgFe(PO_4)_2$, whereas for $KCuFe(PO_4)_2$ at high frequencies an anomaly in the $\varepsilon'(T)$ curve appears at 620 °C. But this anomaly disappears at lower frequencies suggesting that in this case the polarization is due to the mobility of K^+ cations.

4. Conclusion

A new phosphate $KCuFe(PO_4)_2$ was synthesized and found to exhibit an original three-dimensional structure consisted by FeO_6 octahedra sharing corners with Cu_2O_8 units of edge-sharing CuO_5 polyhedra to form ondulating chains extending infinitely along the *b*-axis. The magnetic measurements show this compound to be antiferromagnetic with $C_m=5.71$ emu K/mol and $\theta=-156.5$ K. The electrical properties were compared with those of $KMgFe(PO_4)_2$ featuring a layered structure. With respect to the dielectric behavior of both phosphates with the same stoichiometry and the same monovalent cation as charge carrier, K^+, the respective activation energies are mainly dependent of their structure dimensionality. The 2D magnesium phosphate shows a much lower value of this quantity (0.51 eV) with respect to the 3D copper phosphate (1.22 eV). These results are in accordance with those previously obtained for other potassium monophosphates. For example, $K_2VP_2O_8$ exhibiting a lamellar structure has activation energy of 0.64 eV [24], two orders of magnitude lower than that 1.15 eV, reported for the 3D phosphate $KNi_4(PO_4)_3$ [25].

Appendix A. Supplementary Materials

Supplementary data associated with this article can be found in the online version at doi:10.1016/j.jssc.2011.02.021.

References

[1] H. Ehrenberg, N.N. Bramnik, A. Sensyshyn, H. Fuess, Solid State Sci. 11 (2009) 18.
[2] F. Hatert, A.-M.- Fransolet, W.V. Maresh, Contr. Mineral. Petrol. 152 (2006) 399.
[3] G. Rousse, J. Rodríguez-Carvajal, C. Wurm, C. Masquelier, Chem. Mater. 13 (2001) 4527.
[4] L.N. Komissariva, M.G. Zhizhin, A.A. Filaterov, Russ. Chem. Rev. 71 (8) (2002) 619.
[5] A. Badri, M. Hidouri, M.L. López, M.L. Veiga, A. Wattiaux, M.B. Amara, Solid State Ionics 180 (2009) 1558.
[6] A.A. Belik, F. Izumi, T. Ikeda, M. Okui, A.P. Malakho, V.A. Morozov, B.I. Lazaryak, J. Solid State Chem. 168 (2002) 237.
[7] A.M. Glass, S.C. Abrahams, A.A. Ballman, G. Loiacono, Ferroelectrics 17 (1978) 579.
[8] B.I. Lazoryak, O.V. Bayszhnikova, S.Y. Stefanivich, A.P. Malakho, V.A. Morozov, A.A. Belik, I.A. Leonidov, O.N. Leonidov, V. Tendeloo, Chem. Mater. 15 (2003) 3003.
[9] B.I. Lazoryak, V.A. Morozov, A.A. Belik, S.Y. Stefanovich, V.V. Grebenev, I.A. Leonodov, E.B. Mitberg, S.A. Davydov, O.I. lebedev, V. Tendeloo, Solid State Sci. 6 (2004) 18.
[10] S.Y. Stefanovich, A.A. Belik, M. Azuma, M. Takano, O.V. Bayszhnikova, V.A. Morozov, B.I. Lazoryak, O.I. Lebedev, V. Tendeloo, Phys. Rev. B 70 (2004) 172103.
[11] A. Altomare, G. Cascarano, C. Giacovazzo, A. Guagliardi, J. Appl. Crystallogr. 26 (1993) 343.
[12] G.M. Sheldrick, SHELXL97, A Program for the Solution of the Crystal Structures, University of Göttingen, 1997.
[13] I.D. Brown, D. Altermatt, Acta.Crystallogr. B 41 (1985) 244.
[14] B. Lajmi, M. Hidouri, N. Gmati, A.B. Hammouda, A. Wattiaux, L. Fournés, J. Darriet, M.Ben Amara, Mater. Chem. Phys. 113 (1) (2009) 372.
[15] M. Hidouri, B. Lajmi, A. Wattiaux, L. Fournés, J. Darriet, M.Ben Amara, J. Solid State Chem. 179 (2006) 1808.
[16] W.H. Bauer, Acta Crystallogr. B 30 (1974) 1195.
[17] F. Menil, J. Phys. Chem. Solids 46 (1985) 763.
[18] E. Barsoukov, J.R. MacDonald, Impedance Spectroscopy: Theory, Experiment, and Applications, Wiley Interscience, New York, 2005.
[19] M.M. Ahmad, K. Yamada, Appl. Phys. Lett. 91 (2007) 52912.
[20] D.L. Sidebottom, P.F. Green, R.K. Brown, Phys. Rev. B 56 (1997) 170.
[21] C. Leon, M.L. Lucia, J. Santamaria, Phys. Rev. B55 (1998) 882.
[22] P.B. Macedo, C.T. Moynihan, R. Bose, Phys. Chem. Glasses 13 (1972) 171.
[23] J. Lui, Ch-G. Duan, W.-G. Yin, W.N. Mei, R.W. Smith, J.R. Hardy, J. Chem. Phys. 119 (2003) 2812.
[24] R.J. Grant, I.M. Hodge, M.D. Ingram, A.R. West, J. Am. Ceram. Soc. 60 (1977) 226.
[25] A. Daidouh, M.L. Veiga, C. Pico, Solid State Ionics 106 (1998) 103.